PNAS RESEARCH ARTICLE | NEUROSCIENCE

Transition of the presynaptic vesicle cluster from a compact to dispersed organization during long-term potentiation

Guadalupe C. Garcia[a], Thomas M. Bartol[a], Lyndsey M. Kirk[b], Priyal Badala[a], Kristen M. Harris[b,1], and Terrence J. Sejnowski[a,c,1]

Affiliations are included on p. 9.

Contributed by Terrence J. Sejnowski; received August 18, 2025; accepted April 14, 2026; reviewed by Ege T. Kavalali and Kevin Staras

Long-term potentiation (LTP) is a lasting form of synaptic plasticity that can persist for hours or even days. It is associated with structural changes in both the presynaptic terminal and the postsynaptic spine. Presynaptically, the number and distribution of synaptic vesicles (SVs) affect synaptic efficacy. How the functional changes in synaptic efficacy after the induction of LTP are mirrored by identifiable structural alterations in the SV cluster is not fully understood. Here, we interrogated presynaptic terminals in 3DEM reconstructions from CA3-to-CA1 synapses in *stratum radiatum* of adult rats that had undergone control stimulation, or theta-burst stimulation to produce LTP. An increase was observed in the dispersion of SVs at 2 h after LTP induction. This dispersion resulted in greater distances between neighboring SVs, longer distances to the center of the SV cluster, and an increased variance in SV position relative to the cluster's center. Analysis of the SV clusters distinguished terminals that were potentiated based on their degree of dispersion, distances to neighboring SVs, and SV cluster densities. Our analysis demonstrates that the density of SVs is a property independent of the bouton or SV cluster volumes and is subject to strong regulation. Comparing the spatial distribution of SVs to randomized distributions revealed increased SV mobility following LTP induction. Moreover, theoretical calculations informed by the measured SV cluster densities suggest an increase in the mobility of SVs within the cluster during LTP. These findings provide evidence that the SV cluster undergoes a transition from tight to dispersed, making SVs more mobile during LTP.

long-term potentiation | synaptic plasticity | synaptic vesicles | hippocampal area CA1 | computational model

Significance

Synaptic plasticity, the ability of synapses to change their strength in response to activity, is fundamental to learning and memory, and is accompanied by changes in the presynaptic terminal and the postsynaptic spine. Here, three-dimensional analysis using serial section electron microscopy revealed ultrastructural modifications in the clustering of presynaptic vesicles during long-term potentiation (LTP), a cellular mechanism of learning. LTP resulted in synaptic vesicle clusters being more dispersed. The magnitude of the reduced vesicle density was constant across the range of presynaptic boutons and vesicle cluster volumes during LTP, suggesting this is a tightly regulated property. Biophysical modeling indicated that this regulation could involve reduction of viscosity, supporting elevated vesicle mobility and enhancement of synapse strength during LTP.

Synaptic plasticity is the process by which synapses are modified in structure and function in response to activity, thereby generating a change in synaptic efficacy. Altering the strengths of synapses is essential for learning as it allows neural circuits to adapt to environmental changes. Hence, understanding the interplay of structural and functional changes within synapses during learning may provide new insights into how synaptic strength is regulated.

Long-term potentiation (LTP) is a cellular model of learning that produces a rapid and persistent strengthening of synapses lasting hours to days (1). Converging evidence from recent studies reveals novel presynaptic mechanisms contributing to LTP (2, 3). These include changes in the axonal bouton structure following high-frequency stimulation (4). Two hours after the induction of LTP, there is a decrease in the number of docked and nondocked synaptic vesicles (SVs) (5, 6), paired with an expansion of the presynaptic bouton's surface area (7). This is also accompanied by an increase in release probability (8), with SVs more tightly docked to the active zone (AZ). Redistribution of SVs after LTP was also observed (9). SVs migrate toward the AZ, accompanied by a decrease of the SV density following repetitive hippocampal stimulation (9). After 30 s of prolonged tetanic stimulation, SVs were depleted in the entorhinal cortex for 10 to 60 min (10). Additionally, LTP remodels functional SVs pools (3, 11); specifically, there is an increase in the recycling pool fraction at the expense of the resting pool (11).

In presynaptic terminals, the AZ and SV cluster components have been shown to form biological condensates (12–14). In particular, condensates of synapsin I have been implicated in clustering lipid vesicles in vitro (15) and SVs in vivo (16, 17). SVs are known to interact with several phosphoproteins (18–21) that regulate the state of the SV cluster. The phosphorylation of some of these proteins by synaptic activation could control the clustering of SVs (18, 21).

Here, we used quantitative analysis and a biophysical model to answer the following question: Are there identifiable structural changes in the SV cluster that correlate with

Author contributions: G.C.G., T.M.B., K.M.H., and T.J.S. designed research; G.C.G., T.M.B., and P.B. performed research; G.C.G. and L.M.K. analyzed data; and G.C.G., T.M.B., L.M.K., K.M.H., and T.J.S. wrote the paper.

Reviewers: E.T.K., Vanderbilt University; and K.S., University of Sussex.

The authors declare no competing interest.

[1]To whom correspondence may be addressed. Email: kharris@utexas.edu and terry@salk.edu.

This article contains supporting information online at https://www.pnas.org/lookup/suppl/doi:10.1073/pnas.2522754123/-/DCSupplemental.

Published May 26, 2026.

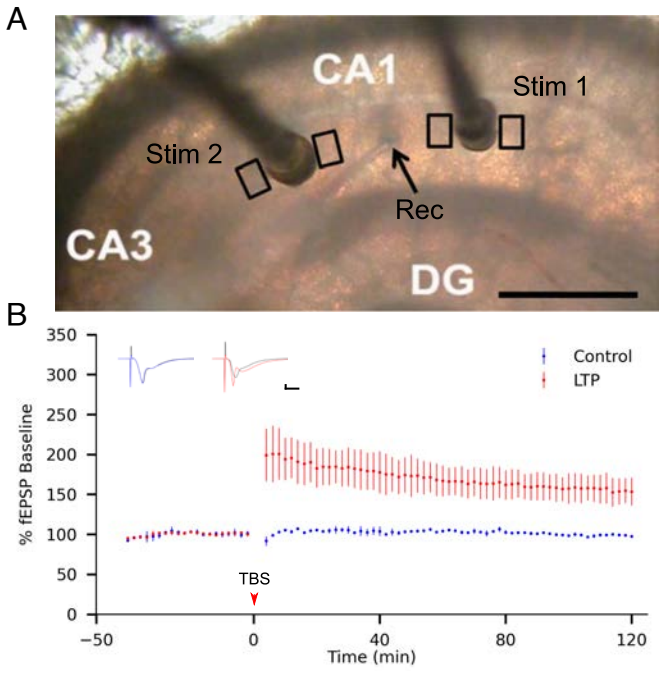

Fig. 1. Induction of long-term potentiation (LTP) via theta-burst stimulation (TBS) in the CA1 stratum radiatum of acute hippocampal slices; stable responses during control and TBS. (*A*) Schematic of an acute hippocampal slice preparation. A recording electrode (Rec) is positioned in the middle of the CA1 s. radiatum, flanked by two stimulating electrodes (Stim 1 and Stim 2) separated by >500 µm. Boxes represent 3DEM sampling regions. The stimulus intensity was set at 75% of the maximum fEPSP, just below the population spike threshold. (Scale bar: 500 µm.) Image adapted from Bourne and Harris, 2011 (22). (*B*) Time course of fEPSP slopes normalized to baseline. At t = 0, LTP was induced via TBS (red), while control stimulation received test pulses only (blue) ($n = 2$ slices from two animals; mean ± SEM). The *Inset* illustrates average waveforms over 10 min from baseline (black, t = −10 to 0 min) and after TBS or control stimulation (red/blue; t = 110 to 120 min). (Scale bars represent 5 ms and 10 mV.)

the change in synaptic efficacy following the induction of LTP? To answer this question, we developed methods to characterize the change in the structure of the SV cluster after LTP induction.

The analysis revealed that following LTP, the SV cluster is less dense, more dispersed, and more similar to a random distribution, while other properties remain unaltered, such as the position of the SV cluster center and the distance from the SVs to the AZ. Moreover, we show that the SV density is uniform across a wide range of SV cluster volumes. Finally, we combined morphological information with a biophysical model to predict the impact of the change in SV density. We provide evidence supporting the hypothesis that SVs in the cluster move faster after the induction of LTP. Altogether, these results provide evidence that the SV cluster undergoes a phase transition during LTP.

Results

LTP Increased Bouton and Mitochondrial Volumes While Decreasing SVs. Acute hippocampal slices were prepared from adult Long-Evans rats. CA3 axons were stimulated in the middle of *s. radiatum* with control test pulses alone or after theta-burst stimulation (TBS) to produce LTP (Fig. 1). Slices were rapidly fixed 2 h later, and tissue near the stimulating electrodes was harvested and processed for serial section EM. In a separate set of experiments, LTP was inhibited by bath-applying 50 µM APV, a selective NMDA receptor antagonist (*SI Appendix*, Fig. S1). Detailed 3D reconstructions of axons, the surface of the postsynaptic density (PSD), and presynaptic mitochondria were generated from 2D contours obtained using annotation software (Fig. 2 *A–D*). The position of nondocked SVs was determined and spherical objects were created around their center point locations. This approach is limited by section thickness of the EM images, which was approximately 60 nm, larger than the average diameter of the SVs (40 nm). To test effects of section thickness, measurements were randomly shuffled around the center of the SVs by ± 31 nm in the z-direction. The percentage error was smaller than 3% and had no effect on the control versus LTP outcomes presented here.

The volumes of the presynaptic bouton were quantified from the 3D axon reconstructions. Boutons with mitochondria (+Mito) and without mitochondria (-Mito) were analyzed separately because synapse areas (as measured by PSD surfaces) were previously shown to be larger on boutons containing a mitochondrion (23). Boutons with mitochondria were significantly larger than those without mitochondria regardless of condition; however, only boutons without mitochondria showed enlarged volumes during LTP (Fig. 2*E* and *SI Appendix*, Table S1).

As previously reported, the number of SVs per bouton were decreased by 30 min, and remained reduced for at least 2 h during LTP (Fig. 2*F*), an effect that was blocked by APV (5–7, 23). The individual SV volumes were calculated from the sampled subsets of boutons and SVs from each series and showed some variability between series (*SI Appendix*, Fig. S2). Using bootstrapping analysis, these distributions were sampled separately for each series to estimate the total SV volume in each bouton. The outcome of the bootstrapping analysis revealed that the total SV volume for each bouton was not changed significantly during LTP (*SI Appendix*, Fig. S3). Mitochondrial volume increased during LTP (Fig. 2*G*) as was previously reported (23). The total mitochondrial volume is moderately correlated with the bouton volume, mainly due to the increase in mitochondrial volume for smaller boutons (Fig. 2*H*). The total SV volume correlated with bouton volume under both control and LTP conditions (Fig. 2 *I* and *J*).

SVs Dispersed During LTP. The Delaunay triangulation method determined all the neighboring SVs for each SV in the cluster (Fig. 3*A*). Pairwise distances between SVs in the cluster revealed mean distances were greater during LTP than under control conditions for boutons with and without mitochondria (Fig. 3*B* and *SI Appendix*, Table S1). The median distance from the SVs to the AZ was unchanged during LTP (Fig. 3 *C* and *D*). Single-synaptic boutons (SSB) had one postsynaptic partner and multisynaptic boutons (MSB) had more than one postsynaptic partner. No significant differences were observed between SSB and MSB within a condition (*SI Appendix*, Figs. S4 and S5).

The mean distance from the SVs to the center of the cluster increased during LTP (Fig. 3 *E* and *F*). Although the center of the SV cluster was farther away from the AZ for boutons with mitochondria, LTP had no effect on this distance (*SI Appendix*, Fig. S6 and Tables S1 and S2). The SD of SV positions from the cluster center revealed SVs were more dispersed during LTP (Fig. 3 *G* and *H*). Overall, these results indicate that SVs are more widely dispersed during LTP.

SV Cluster Volume Was Maintained During LTP. The SV cluster volume was estimated by forming and meshing the convex hull, defined as the smallest convex shape containing all the SVs (Fig. 4*A*). The total SV cluster volume was not significantly altered despite the loss of SVs during LTP (*SI Appendix*, Table S1).

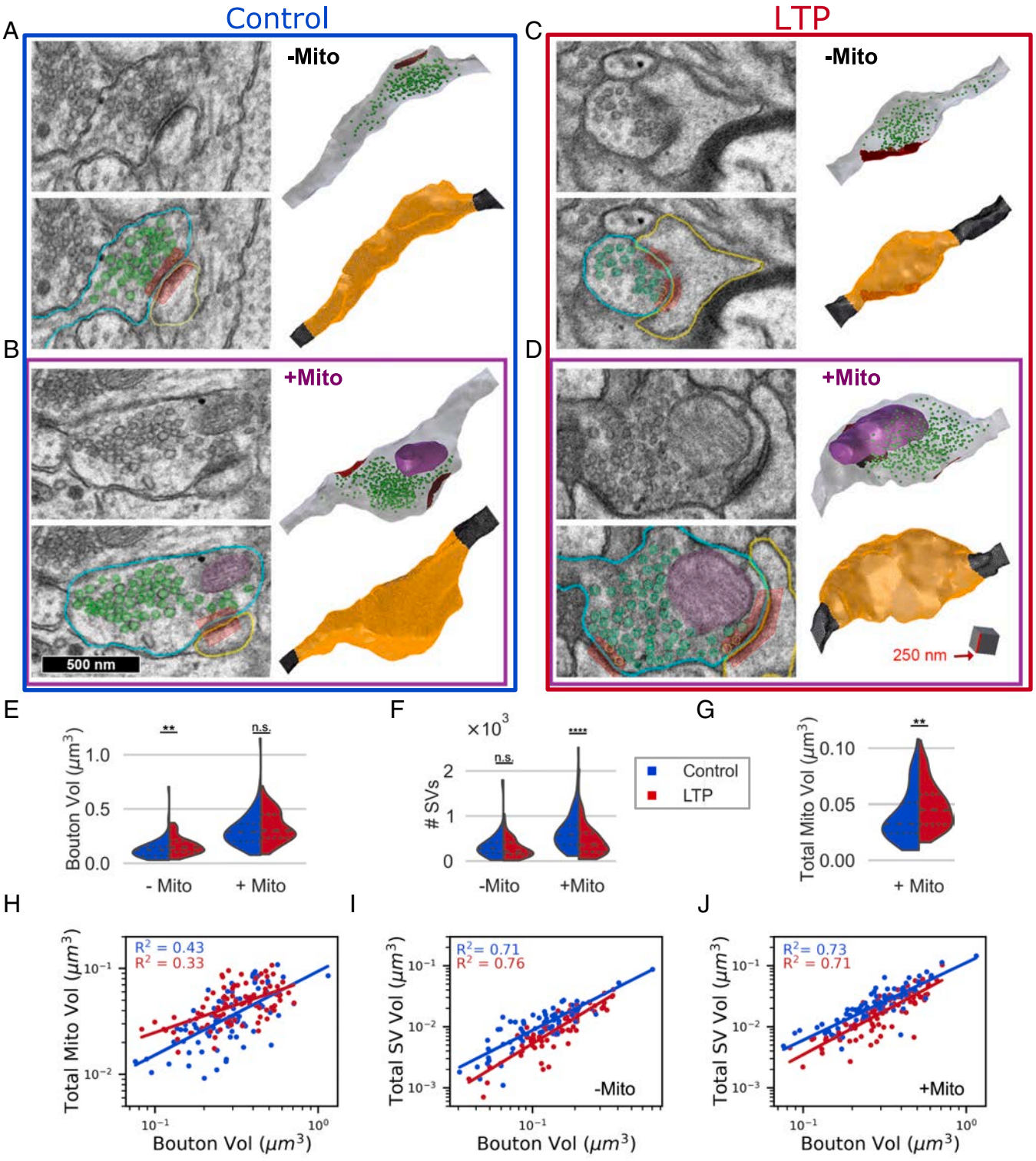

Fig. 2. LTP increases bouton and mitochondrial volume, and reduces SV numbers relative to the control condition. EM images of representative boutons and their 3D reconstructions: (*A* and *B*) under control and (*C* and *D*) LTP conditions without mitochondria (-Mito) and with mitochondria (+Mito). SVs are represented as green spherical objects ranging from 20 to 24 nm in diameter based on mean calculations for each series, see *SI Appendix*, Fig. S2*A*. Mitochondria are magenta, and active zones with their associated PSDs are encircled in red. The surface area of the bouton is highlighted in orange in the 3D reconstructions. (*E*) The volume was greater for +Mito than -Mito boutons ($P_{control} < 8.8 \times 10^{-16}$; $P_{LTP} < 5.2 \times 10^{-14}$, yet only -Mito boutons were enlarged during LTP ($P_{-Mito} < 0.004$; $P_{+Mito} < 0.087$). (*F*) The number of SVs per bouton decreased after LTP. (*G*) Total mitochondrial volume increases after LTP. (*H*) Correlation between the bouton volume with the total mitochondrial volume (ANCOVA test $P < 1 \times 10^{3}$, $\eta^2 = 0.06$). (*I* and *J*) Correlation between the bouton volume with the total SV volume for -Mito and +Mito boutons (-Mito, ANCOVA test $P < 1.38 \times 10^{-7}$, $\eta^2 = 0.2$ and +Mito, ANCOVA test $P < 1.09 \times 10^{-8}$, $\eta^2 = 0.18$). Violin plots (*E*–*G*) show quartiles 25th, 50th, and 75th. Significant differences are indicated as $^{**}P < 0.01$ and $^{****}P < 0.0001$. Medians, SDs, and *P*-values are in *SI Appendix*, Table S1.

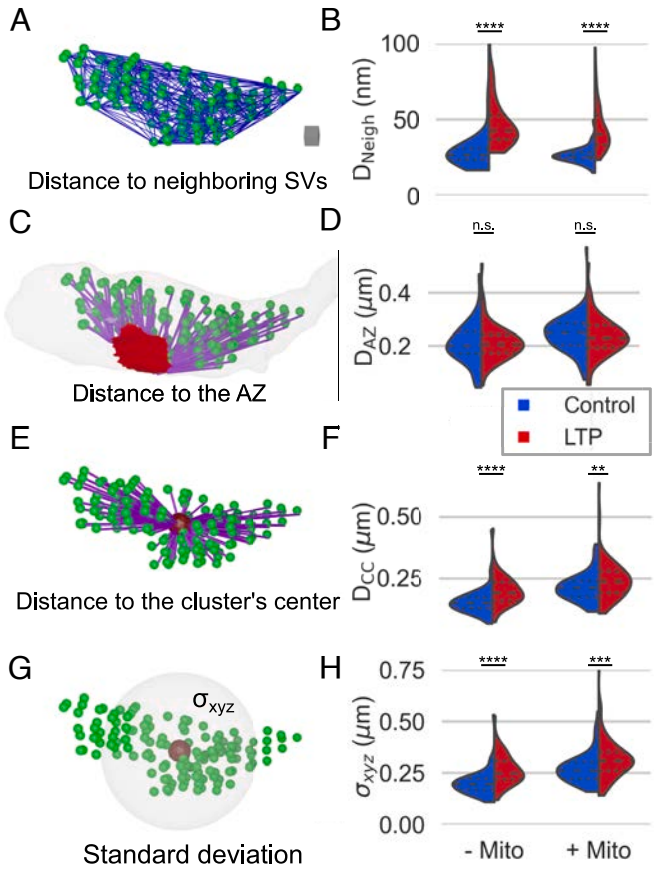

Fig. 3. SV dispersion during LTP. (*A*) Delaunay triangulation for a representative SV cluster showing distances (blue lines) between neighboring SVs (green spheres). (*B*) The mean distance between neighboring SVs (D_{Neigh}) increased during LTP for -Mito and +Mito boutons. (*C*) Distances (purple lines) from the SVs to the active zone (red, AZ). (*D*) Distances from the SVs to the AZ (D_{AZ}). (*E*) Distances (purple lines) from the SVs to the center of the cluster (CC, large red circle). (*F*) SVs are farther from the center of the SV cluster (D_{CC}) during LTP. (*G*) SD (σ_{xyz}) of SV positions from the CC. (*H*) SVs are more dispersed during LTP. (Scale cube in a for *A*, *C*, *E*, *G* = 0.001 μm^3. Violin plots show 25th, 50th, and 75th quartiles. Significant differences are $^{**}P < 0.01$,$^{***}P < 0.001$, and $^{****}P < 0.0001$. Medians, SDs, and *P*-values are in *SI Appendix*, Table S1.

The cluster-associated volume was calculated by subtracting the estimated total SV volume from the SV cluster volume for each bouton (Fig. 4*B*). The cluster-associated volume increased for boutons without mitochondria during LTP but was maintained for boutons with mitochondria (Fig. 4*C*). The SV cluster density was calculated by dividing the number of SVs by the cluster-associated volume and was decreased during LTP for boutons both lacking and containing mitochondria (Fig. 4*D*). Since many SVs were lost during LTP, and the cluster-associated volume was increased or stable, it is not surprising that the SV cluster density decreased during LTP relative to control conditions (*SI Appendix*, Table S1).

Regulation of Individual SV Density by Condition. To define the spatial domain of each SV, we generated Voronoi tessellations that partitioned the total SV cluster volume into discrete, vesicle-specific regions (Fig. 4 *E* and *F*). The SV-associated volume was calculated by subtracting the individual SV volumes from its Voronoi volume (Fig. 4*G*). The SV-associated volumes were greater with LTP regardless of the presence or absence of mitochondria (Fig. 4*H*). The individual SV density, calculated as the inverse of the SV-associated volume, was reduced during LTP (Fig. 4*I*). Although the SV cluster volume scaled with bouton volume (Fig. 4*J*), the individual SV density was constant across boutons (*SI Appendix*, Fig. S7) and SV cluster volumes for control and LTP conditions, but lower overall during LTP (Fig. 4*K*).

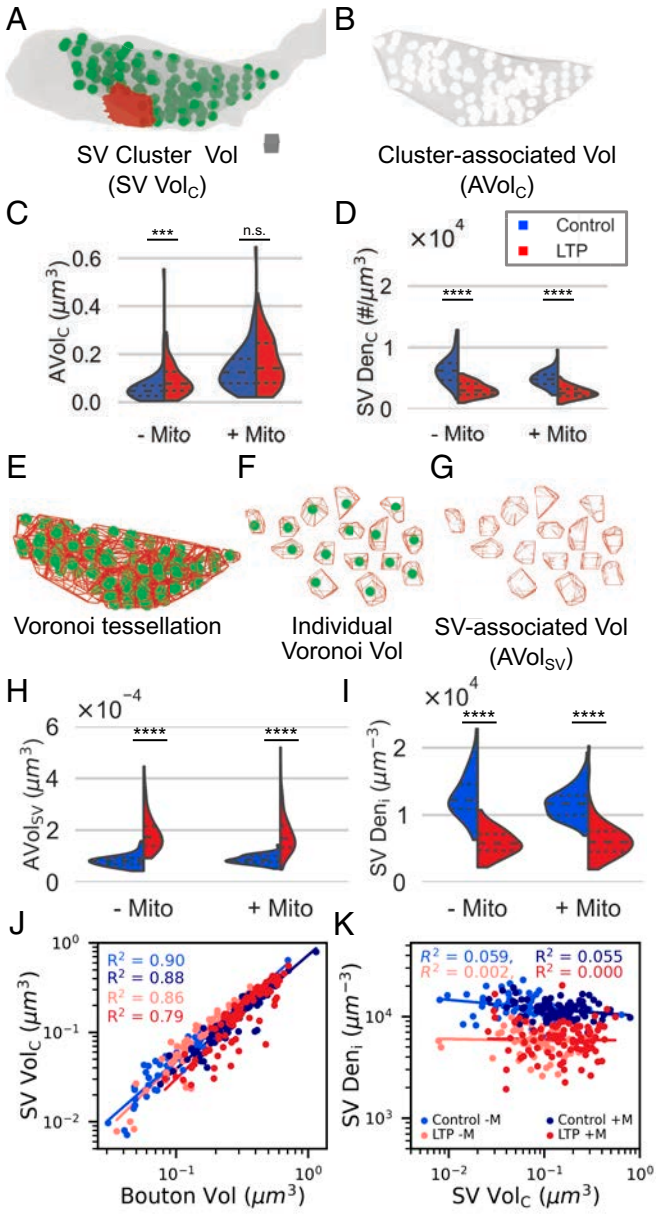

Fig. 4. Cluster volume maintained while SV density is reduced with LTP. (*A*) Minimal volume of the SV cluster (SV Vol_C) calculated using the convex hull method. This estimate accounted for the diameter of SVs at the edge of the convex hull, and subtracted volume that intersected with mitochondria. (*B*) The cluster-associated volume ($AVol_C$) is what remained after subtracting the total SV volume. (*C*) The cluster-associated volume increased in -Mito boutons but not +Mito boutons during LTP. (*D*) The SV cluster density (SV Den_C) was calculated as the total number of SVs in the bouton divided by the cluster-associated volume and decreased during LTP. (*E*) Voronoi tessellation (red) of a SV (green) cluster. (*F*) Individual Voronoi volumes around example SVs from that cluster. (*G*) SV-associated volumes ($AVol_{SV}$, calculated subtracting the SV volume to the individual Voronoi volume). (*H*) SV-associated volumes increased with LTP. (*I*) The inverse of the SV-associated volume, i.e., individual SV density (SV Den_i), decreased during LTP. (*J*) The SV cluster volume scaled with bouton volume. (*K*) The individual SV density was constant across SV cluster volumes, but decreased with LTP. (Scale cube in a for *A*, *B* = 0.001 μm^3. Violin plots show quartiles 25th, 50th, and 75th. Significant differences are indicated as $^{***}P < 0.001$, and $^{****}P < 0.0001$. Medians, SDs, and *P*-values are in *SI Appendix*, Table S1.

Thus, the individual SV density was a property independent of the SV cluster or bouton volumes; it remained constant over a range of three orders of magnitude of the SV cluster volume for each condition, suggesting a specific regulatory mechanism.

Spatial Organization of SVs at Synapses. The distribution of Voronoi areas (in 2D) and volumes (in 3D) provide information about the spatial distribution of the components in space (24). For instance, the distribution of Voronoi areas (in 2D) has been used to identify clusters of proteins from superresolution images (25, 26). When points are regularly distributed, the Voronoi volumes do not vary much. However, when points are clustered, the volumes are highly variable. To illustrate this effect, we presented the 2D Voronoi tessellations for a set of random, clustered, and uniformly distributed points (Fig. 5*A*). Smaller Voronoi areas occur when points are clustered in space (Fig. 5*A*). The measured spatial distribution of SVs was compared with a random distribution of SV in each bouton (Fig. 5 *B* and *D*). Under both control and LTP conditions the SV-associated volumes were smaller than random distributions, suggesting SVs were clustered (Fig. 5 *C* and *E*).

Considering densities rather than volumes, the SV cluster and the individual SV densities are equal only for uniform distributions of points (Fig. 5*A*). The individual SV density was greater than the cluster density in both conditions (Fig. 5*F*), presenting the largest values for control conditions. This suggests SVs are tightly clustered under control conditions. The individual SV densities for the random distributions of SVs were also greater than the cluster densities under both conditions (Fig. 5*F*), showing more similar values as they resemble uniform distributions.

The median SV-associated volumes are consistently smaller when comparing the original distributions to the random distributions (Fig. 5*G*). This suggests that the spatial distribution of SVs is not random. During LTP, the medians begin to approach those of the random distributions (Fig. 5*G*), indicating that SVs in the cluster shifted closer to a random pattern, resulting in a less clustered arrangement.

Distinguishing Potentiated Synapses by SV Organization. So far, changes in SV organization were assessed individually. However, when considered together, for instance, the distances to neighboring SVs and SV density demonstrate a high correlation (Fig. 6*A*). Principal component analysis (PCA) in combination with clustering methods tested whether LTP-related changes in the distances to neighboring SVs, SV densities, dispersion of the SV cluster, and bouton volume together effectively distinguish potentiated synapses. To cluster boutons with similar properties, first PCA was used to identify the variables that better capture the variability of the data. Afterward, the K-means algorithm was employed to cluster the boutons with similar properties (Fig. 6*B*). We predict that boutons with larger distances to neighboring SVs, lower densities, and greater dispersion from the center of the SV cluster are those that have been potentiated. Therefore, we refer to this group as potentiated boutons, while the other is termed stable (Fig. 6*B*). Separate analyses were performed for boutons lacking and containing mitochondria, since some structural features showed differences across these populations. Additionally, while the volume of the boutons increases, this change reaches statistical significance only in terminals that lack mitochondria. The labels obtained after applying the clustering method were mapped to the original values (Fig. 6*B*). Furthermore, we examined the structural features of APV-treated synapses and confirmed that their values overlapped with those of control synapses (*SI Appendix*, Fig. S8).

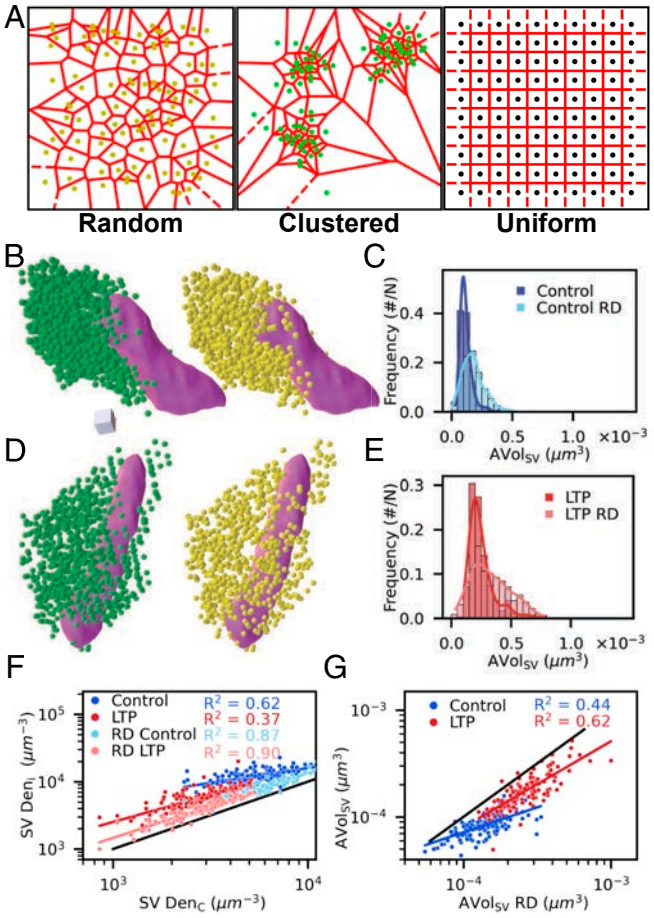

Fig. 5. Spatial organization of SVs at synapses. (*A*) 2D Voronoi tessellations (red lines) for random (yellow), clustered (green), and uniform (black) distributions of points. Smaller Voronoi sizes are observed for clustered points. (*B*) Representative examples of a SV cluster under control conditions (green spheres) and random distributed (RD) SVs (yellow spheres). Scale cube = 0.001 μm^3. (*C*) Smaller SV-associated volumes ($AVol_{SV}$) are observed for the original distribution (in blue) compared to random distributed SVs (in light blue). (*D*) Same as in (*B*) for a SV cluster under LTP conditions. (*E*) Same as (*C*) for a SV cluster under LTP conditions. Smaller volumes are observed for the original distribution of SVs. (*F*) Individual SV vs. Cluster SV densities at each bouton under control in blue and under LTP conditions in red, to provide a reference for comparison against a uniform distribution, a black line with a slope and intercept equal to one was included. The Individual SV density is greater than the SV cluster density under both conditions, with larger values observed under the control condition. This indicates that SV are more compact in control conditions. For random distributed (RD) SVs, the densities are more similar, as is expected, since they resemble a uniform distribution more closely. (*G*) Median SV-associated volume for the original vs. random distributed SVs. During LTP, the distribution of SV is more similar to a random distribution of SVs.

Theoretical Outcomes Suggest SV Mobility in the Cluster Increased During LTP. We explored the potential implications of the change in SV cluster density from control versus LTP conditions using theoretical calculations and a biophysical model. To illustrate the effect, a 3D reaction–diffusion model of the axon and the SV cluster with SVs diffusing in 3D space (Fig. 7*A*) was considered; the model was implemented in MCell4, an agent-based reaction–diffusion simulator (27). The theoretical calculations were informed by the SV cluster densities and an experimentally measured diffusion coefficient in the SV

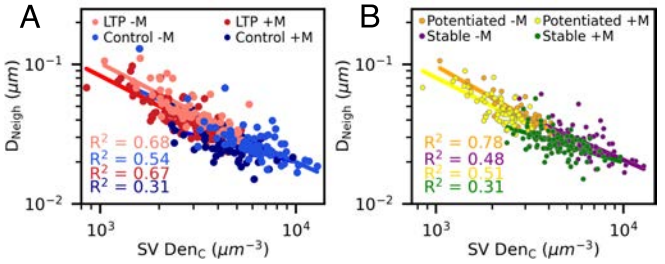

Fig. 6. Potentiated synapses have lower SV densities, larger distances to neighboring SVs, and are more dispersed from the cluster's center. (*A*) Distances to neighboring SVs (D_{Neigh}) vs. SV cluster density (SV Den_C) under control conditions in light blue (-M) and dark blue (+M), and under LTP in salmon (-M) and red (+M). (*B*) Two populations of boutons are identified using five features of the SV cluster employing the K-means clustering algorithm, using the first two principal components of PCA. The potentiated population has a lower density, higher distance to neighboring SVs, higher SV-associated volume, and SV are more dispersed from the center while the opposite occurs in the other population.

cluster (16) to determine the other diffusion coefficients. Thus, the diffusion coefficient for SVs in the axon was estimated based on these assumptions and held constant between control and LTP conditions (Methods, *SI Appendix*, Tables S4 and S5).

Under these assumptions, conditions for control and LTP can be compared. During LTP, the SV cluster density roughly halved, suggesting that the ratio of the diffusion coefficients between the axon and SV cluster must be 1:4, which translates to a D_{LTP} of approximately 0.2 $\mu m^2 s^{-1}$ (*SI Appendix*, Table S1 and Eq. **S1**). The modeling approach illustrates how the number of SVs within the cluster is maintained due to the difference in diffusion coefficients between the axon and the SV cluster (Fig. 7*B*, before 2.5 s). The increase in diffusion coefficient of the SV cluster by a factor of 4 produced the observed halving in SV number in the cluster for boutons with mitochondria, while boutons without mitochondria experienced a smaller decrease (Fig. 7*B*, after 2.5 s). For boutons lacking mitochondria, the expansion of the SV cluster was considered, which resulted in a smaller reduction in SV number in the cluster (Fig. 7*B*).

In summary, comparing biophysical models with different diffusion coefficients with measured SV cluster densities suggests that the mobility of SVs in the cluster increases during LTP. Although the SV densities for boutons containing and lacking mitochondria differ, the density ratios under control and LTP are approximately half for both, implying similar changes in the diffusion coefficients in boutons containing and lacking mitochondria.

Discussion

Cluster-associated volume was maintained across the LTP and control conditions, the distances between neighboring SVs increased, SVs were more dispersed from the cluster's center, and the SV-associated volume increased. In contrast, the SV cluster center and the distance from the SVs to the AZ did not differ between the LTP and control conditions. The distances between neighboring SVs and the SV-associated volume were altered by LTP whether or not a mitochondrion was present in the bouton. However, the degree of dispersion of the SVs from the cluster's center and the cluster-associated volumes were greater when a mitochondrion was present in the presynaptic bouton.

In principle, snapshots of synapses do not provide clear identification of which synapses were potentiated. However, the detailed quantification of synapses from control and LTP conditions suggest a collection of properties distinguishing potentiated presynaptic terminals. Namely, potentiated synapses have SVs more dispersed, with larger distances to neighboring SVs and lower SV cluster densities. All of these characteristics show statistically significant differences between the potentiated and stable groups. In other words, these SV measurements are biomarkers for recent (2 h) LTP. Additionally, while the bouton volumes increase, these changes reach statistical significance only in terminals that lack mitochondria. A similar trend is observed in the overall PSD (23). Meanwhile, the decrease in the total SV number is statistically significant only for boutons that have mitochondria. Using this approach, 37 synapses transitioned from LTP to a stable state, representing 12% of the total synaptic population. Furthermore, to test our hypothesis, we compared the distances to neighboring SVs and the SV density of control and LTP synapses with those of APV-treated synapses (*SI Appendix*, Fig. S8). We found that they mainly overlap with the control population.

The individual SV density, or its equivalent median SV-associated volume, remained constant across a range of three orders of magnitude in SV cluster volume for a given condition. This finding suggests that this intensive property of the SV cluster is likely under strong regulation. New perspectives on the regulation of the SV cluster have recently emerged that might shed light on the underlying biophysical mechanisms. Biological condensates have been implicated in clustering lipid vesicles in vitro (15) and SVs in vivo (16, 17). Several phosphoproteins participate in regulating the SV cluster (18–21). Notably, the phosphorylation of synapsin I by protein kinases after synaptic activation dissociates synapsin from SVs and initiates the mobilization of SVs (18, 21). Condensates are thought to undergo phase transitions, similar to how matter changes between different states (28). During such transitions, a control parameter governs the change from one phase to another, leading to changes in the intensive properties of the system. Posttranslational modifications are an essential control mechanism of phase transitions (29). During LTP, the individual SV density, an intensive property of the SV cluster, changed in analogy to a phase transition. This has significant functional implications, as this transition inhibits the recycling of SVs (7).

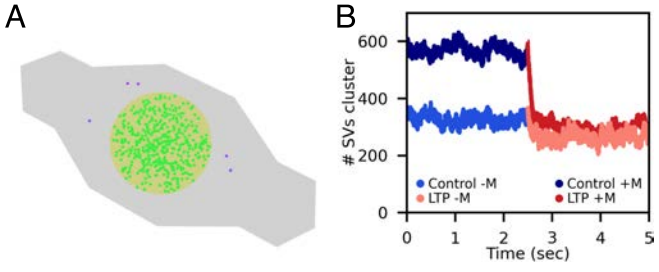

Fig. 7. 3D reaction–diffusion simulations illustrate the effect of differential diffusion in the SV cluster versus axonal cytoplasm. (*A*) In the computer simulations SVs diffuse with different coefficients in the axon (purple spheres) compared to the SV cluster (green spheres). A gradient in the SV density can be maintained in this manner. (*B*) Theoretical calculations based on observed changes in SV densities, predict an alteration in the diffusion coefficient during LTP. Accordingly, in the computer simulations, the diffusion coefficient was adjusted within the SV cluster (at 2.5 s) to emulate LTP conditions. Calculations for boutons lacking (-M) and containing (+M) mitochondria were performed separately, because their measured SV densities vary. Additionally, in the simulations for boutons lacking mitochondria, an expansion of the SV cluster volume by about 50% was considered during LTP, which reduces the difference in the SV number in the cluster relative to control conditions. Although the change in the diffusion coefficient from control to LTP is similar in both instances, the decrease in SVs differs.

The size of subcellular organelles is tightly controlled (30, 31). Scaling relations indicate potential mechanisms for size control, which may arise from genetically programmed pathways, relative growth, or physical constraints (31). In mammalian cells, mitochondrial cytoplasmic occupancy remains relatively constant (32). Although the scaling of subcellular organelles with bouton volume has been well studied in various brain cell types (33–35), we showed that the SV cluster volume is also tightly regulated. It scales with the bouton volume, as do other SV cluster properties such as SV number and total SV volume. The correlation between mitochondrial and bouton volume decreases during LTP due to an increase in mitochondrial volume in the smaller boutons only.

Using theoretical calculations and a biophysical model, we predicted the implications of the change in SV density at synapses. The calculations allowed us to estimate the change in diffusion coefficient (or viscosity) from the axon to the SV cluster. Our findings are consistent with measurements observed in other condensates (36). This approach led to the outcome of an increment in the mobility of SVs in the cluster during LTP. Moreover, we observed that the distribution of SV-associated volumes during LTP more closely resembled random distributed SVs. This similarity suggests that SVs may be gaining mobility during LTP. A recent work developed methods to measure the viscoelastic properties of synapsin 1 condensates in cells (37). They found that the viscosity of the condensates can be regulated by the SV concentration (or density), with a higher concentration of SVs having a higher viscosity implying a lower diffusion coefficient. These results align with our findings.

During periods of low activity, docked SVs are recruited for fusion. However, during periods of prolonged stimulation, it becomes necessary to recruit SVs from the resting pool (3, 11), a process mediated by Calcineurin activity (3). Although we cannot access functional SV pools with EM images, we believe this process may be facilitated by the decrease in viscosity within the SV cluster and the increase in mobility of the SVs, as reported in this study. These changes may allow other proteins to bind to SVs, preparing them to join the ready-releasable pool of SVs. Increased SV mobility could affect the rate at which synapses respond to a depletion of the ready-releasable pool of SVs, in particular if the retrieval of SVs is inhibited.

The concentrations of synapsin I and alpha-synuclein have been proposed to regulate the SV cluster, affecting the phase, density, and volume of the condensate (38). However, their relevance during LTP remains a subject of ongoing debate. LTP remained unaffected in both double and triple synapsin-knockout (KO) models (39, 40). Similarly, KO mice that lack alpha or/and beta synucleins show no effect in short or long synaptic plasticity (41). Nevertheless, genetic manipulation of synucleins has been shown to cause compensatory changes in the expression levels of synapsin and other presynaptic proteins (42). It remains to be determined whether acute synuclein or synapsin knockout yields comparable results. Interestingly, mice with synapsin 1 and 2 knockouts have short-term forms of plasticity affected (39). This may be explained by different subtypes of NMDA receptors mediating different forms of plasticity (43). One could hypothesize that the kinetic properties of the different NMDA receptor subtypes might translate into different sensitivity to alterations of presynaptic glutamate release.

As detailed in the Methods section, we observed some variability in the sampled SV radii in each animal (*SI Appendix*, Fig. S2). For this reason, we did not combine these distributions together and instead extracted estimates of the SV radii and total SV volume for each condition and animal for downstream analysis. The most relevant measured quantities in this study are the SV densities. These values are central to the mathematical model developed and crucial for predicting the change in viscosity within the SV cluster. These quantities are statistically significant in both animals. For the eight measured or derived quantities presented in Figs. 3 and 4, only three quantities—specifically, the distance to the cluster's center, the SD, and the cluster-associated volume—did not show statistical significance in one animal for boutons containing mitochondria, while the other animal did exhibit statistical differences. Data from both animals are presented together to provide a clearer overview of the observed effects. However, these discrepancies raise compelling questions for future investigation. Since one animal exhibited larger SV radii, larger mitochondria, and larger distances between SVs after LTP induction, this suggests a link between mitochondria and the response to LTP, as has been recently shown for MF synapses (44). We consider these questions should be better addressed in the future with higher-resolution images such as by combining EM tomography with wide field scanning electron microscopy electron tomography (45).

LTP modifies the clustering of SVs. It would be valuable to investigate whether similar responses occur in young and adult animals during the natural aging process. Aging is the primary risk factor for most neurodegenerative diseases, including Alzheimer's disease (AD). The modulation of the SV cluster has been reported in AD models (46). Furthermore, the study of the material properties of condensates is an active area of research (47), which has been linked to age-associated diseases. Furthermore, developing a multiscale model that captures the interaction of SVs with proteins regulating the clustering will be an invaluable tool to explore the functional implications of condensate formation on synaptic transmission and help pinpoint the fundamental protein–protein interactions driving this process. Uncovering the molecular mechanisms underlying SV clustering is fundamental to understanding synaptic transmission, learning, and memory.

Materials and Methods

Animals. All animal procedures were approved by the Institutional Animal Care and Use Committee at The University of Texas at Austin and adhered to NIH guidelines for the humane care and use of laboratory rats.

Slice Preparation, Electrophysiology, and Microwave Fixation. Methods for slice preparation and electrophysiological recordings followed previously described protocols (5, 22). Briefly, following halothane anesthesia, adult male Long-Evans rats (postnatal days 60 to 61) were killed via decapitation. Brain slices 400 μm thick were collected from the middle third of the hippocampus at room temperature using a Stoelting tissue chopper (4 animals; 1 slice per animal). Slices were maintained in a humidified interface chamber for a 3-h recovery period at 32 °C, during which they were continuously perfused with artificial cerebrospinal fluid (aCSF). In the experiments where LTP was blocked, 50 μM APV (D-2-amino-5-phosphonopentanoic acid; Sigma Aldrich, St. Louis, MO) was added to the aCSF after the initial 3-h recovery period and remained present throughout the experiment. Two concentric bipolar electrodes were lowered into the middle of *stratum radiatum* in area CA1 (22) separated by >500 μm with a recording electrode positioned between them (Fig. 1). The experimental design was counterbalanced across two sessions to prevent electrode-specific bias. TBS and control were delivered on opposite ends of the hippocampal slice (near CA3 or subiculum), and pulses from each stimulating electrode were alternated. In one experiment, Stim 1 served as the control while Stim 2 received the TBS protocol; these assignments were reversed in the other experiment, with Stim 1 receiving TBS and Stim 2 serving as the control, to account for any bias across the CA1 field. A stimulus–response input–output (I/O) curve was generated by

measuring the initial slope of the field excitatory postsynaptic potential (fEPSP) (Fig. 1). The intensity of the stimulus was set at 75% of the maximum fEPSP, below the population spike threshold. It was maintained at this constant level for the duration of the experiment. Stimulation was applied once every 2 min, with a 30-s interval between control and LTP stimulation electrodes. Baseline recordings were collected from each stimulating electrode every 2 min (offset by 30 s) for 30 min. TBS was delivered to one stimulating electrode at time 0 to produce LTP (Fig. 1). TBS consists of 8 trains delivered at 30 s intervals; each train comprises 10 bursts (5 Hz), with 4 pulses per burst (100 Hz). fEPSPs were recorded for 2 h in response to alternating pulses from control and LTP stimulating electrodes. To account for potential site-specific effects, the positions of the control and LTP-inducing electrodes (placed near CA3 or the subiculum) were alternated across experiments (Fig. 1*A*).

Fixation and Processing for EM. Tissue fixation and imaging protocols followed previously published procedures (22). Within 1 min of the last recording, electrodes were removed and hippocampal slices were rapidly fixed by immersing them into a mixed aldehyde fixative (6% glutaraldehyde and 2% paraformaldehyde in 0.1 M cacodylate buffer with 2 mM CaCl2 and 4 mM MgSO4) and microwaving the slice in fixative for 10 s. Slices were maintained in fixative overnight at room temperature. Following fixation, the tissue was embedded in 7% agarose and sectioned at a thickness of 70 μm using a vibratome (Leica WT 1000S, Leica, Nussloch, Germany). To prepare for EM, the vibra-slice containing the electrode indentation and two vibra-slices were processed in a 1% osmium/1.5% potassium ferrocyanide mixture followed by 1% osmium alone. Samples were then dehydrated through graded ethanol (50 to 100%) and propylene oxide, embedded in LX112, and placed in a 60 °C oven for 48 h. From each experiment, three samples were obtained spanning the regions beside and beneath the stimulating electrodes. The absolute positions of the samples were located 150 to 200 μm away from the stimulating electrode tips, at a depth of 120 to 150 μm from the slice air surface (Fig. 1). Thin sections were mounted on Pioloform-coated slot grids (Synaptek, Ted Pella). Sections were counterstained with saturated ethanolic uranyl acetate and Reynolds lead citrate and imaged on a JEOL 1230 electron microscope with a Gatan digital camera at 5,000X magnification. Following an assessment of tissue preservation quality, approximately 200 serial sections were collected and imaged. To ensure unbiased analysis, experimental conditions were masked using a five-letter code. To calibrate X-Y dimensions, a diffraction grating replica (Ernest Fullam, Latham, NY) was imaged with each series. Serial sections were imported into Reconstruct (48), and aligned.

Bouton Inclusion Criteria and Unbiased Analysis. Five dendrites of similar caliber and their synapses were previously segmented using Reconstruct software (48). Section thickness was determined using the cylindrical diameters method, calculated by dividing the diameters of longitudinally sectioned mitochondria by the number of sections they spanned (49). Fifteen excitatory spine synapses were identified, and their corresponding axons were reconstructed through manual tracing. Axonal boutons were traced extensively to encompass both the target bouton and the flanking interbouton segments (7). When a neighboring spine made a synapse onto the same bouton its associated synapses were also traced. Nondocked vesicles were stamped and mitochondria were traced.

3DEM Reconstructions. EM images and traces were visualized in the new version of Reconstruct (48) (PyReconstruct) (50). 3D reconstructions of axons and mitochondria were generated using the NeuropilTools addon for Blender (version 2.79) (51). The program Contour Tiler (52), which is integrated into NeuropilTools, produced triangulated surface meshes from the 2D traced contours. The resulting 3D meshes were improved using the GAMer module to smooth and remove distortions. The positions of the SV center were also imported into Blender. Synaptic contact areas were delineated on the axon surface area via the object tag region module in NeuropilTools.

Quantification of Axonal Bouton Morphology. Axonal morphology was evaluated in 3D by two blinded observers to facilitate comprehensive visual inspection (7). Bouton regions were manually circumscribed using the NeuropilTools lasso tool (Fig. 2 *A*–*D*). Bouton boundaries were defined at the point where axonal diameter stabilized into a relative uniform, tubular circumference, marking the transition to the interbouton region. To ensure accurate delineation, mitochondrial positioning, SV distribution, and synaptic contacts were used as contextual markers, particularly at the transition between the axonal bouton and interbouton regions.

Surface area measurements were performed in duplicate by two masked experimenters to determine intra- and intertracer error. Any measurement showing a variance greater than 10% triggered a joint review to identify the source of the error. We also established strict exclusion criteria for boutons with poorly defined boundaries or irregular morphologies, including cases of apparent merging or splitting. The mean intratracer and intertracer errors for surface area measurements were $2.04\% \pm 0.08\%$ and $2.43\% \pm 0.14\%$, respectively. For all subsequent analyses, the mean value of the four independent surface area measurements was utilized. A total of 297 boutons were analyzed: 81 were boutons under control conditions with mitochondria, 61 without; 88 boutons were under LTP conditions with mitochondria, and 67 without.

Quantification of SV Surface Area and Volume. A subset of the SVs was manually traced from each dataset to estimate the total SV volume at each bouton. The circumference of a selected subset of SVs was measured, and their radii were calculated, assuming SVs are circular. As surface area was derived from circumference measurements, inclusion was restricted to SVs that exhibited a strictly circular morphology, were clearly resolved from neighboring structures, and were entirely contained within a single section to avoid truncation artifacts. To ensure a representative sample of bouton sizes and conditions for vesicle analysis, axonal boutons in each series were first stratified by the presence or absence of mitochondria. Within these two populations, boutons were ranked by surface area and partitioned into 10% deciles. One bouton was randomly selected from each decile; if it contained at least 10 SVs meeting our inclusion criteria, these SVs were segmented and their spherical surface area calculated from the measured circumference. If the initial selection failed to meet this 10-SV minimum, a surrogate bouton was randomly drawn from the same size bin. In total, SV tracing was performed on 30 mitochondria-containing and 30 mitochondria-lacking boutons per series (*SI Appendix*, Fig. S2; $n = 8$ series, 480 boutons, 8,629 SVs). From these measurements the individual SV volume was estimated for each dataset, assuming SVs are spherical (*SI Appendix*, Fig. S2).

Total Vesicle Volume. Subsequently, bootstrapping analysis was performed to estimate the total SV volume and its error for each bouton. For each bouton, a number of individual SV volumes was randomly selected from the volume distribution with replacement, where the number selected corresponds to the number of SVs in that bouton. The values were then summed to provide an estimate of the total SV volume. The individual SV volume distributions were categorized by animal, experimental condition, and whether the boutons contained mitochondria. This procedure was repeated N times for each bouton. The mean of the N values was used to estimate the total SV volume at each bouton (Fig. 2*G*), where N was set as 10.000.

Morphometric and Statistical Analyses. Several Python scripts were developed to analyze the distribution of SVs in 3D in Blender 2.79. All the measured quantities are stored in a csv file in the repository (54), along with the generated scripts (in the folder named scripts_blender). To further analyze and plot these measurements another set of scripts was developed, using Python 3.9.19, Scipy version 1.11.4, Numpy version 1.21.6., Pandas version 1.4.0, Matplotlib version 3.8.2, Seaborn version 0.11.2, and Sklearn version 1.3.2. All the associated material can be found in the repository (in the folder scripts_figures). Statistical significance between distributions was assessed using the nonparametric Mann–Whitney–Wilcoxon test implemented in SciPy.

Distance to Neighboring SVs. To determine the distance to neighboring SVs, the Delaunay triangulation for each SV cluster was generated. For a given set of points, the Delaunay triangulation is such that no point in the set is inside the circumcircle of any triangle in the triangulation. Neighboring SVs are connected vertices in the Delaunay triangulation. The Euclidean distance between neighboring SVs was calculated and the mean distance was computed

for each SV. The triangulation was generated using the associated routine in Scipy, through a Python script written for Blender 2.79. Finally, the median was computed from these distributions of distances, which is the final quantity reported for each bouton. Two times the median radius of the SV was subtracted to compute the final distance, which we refer to as the distance to neighboring SVs throughout the manuscript. The median radius of the SVs for each animal, condition, and boutons containing and lacking mitochondria was estimated using bootstrapping analysis based on the sampled SV surface areas. This analysis is similarly to the one used for the total SV volume, but these quantities are now for the population under the same conditions.

SV Cluster Volume. SV cluster volumes were estimated by calculating the convex hull, which is the smallest convex set that contains all SV centers for each identified cluster. This effectively creates a geometric envelope that represents the spatial extent of the cluster. We used the ConvexHull routine in Scipy for this calculation. Afterward, the associated 3D mesh was generated in Blender. The Blender's "Boolean Difference Modifier" was then used to subtract the intersection of the mitochondria and the axon with the convex hull from the convex hull volume. Finally, the resulting convex hull volumes and surface areas were calculated employing the meshalyzer plug-in in CellBlender (51). Since the initial convex hull calculations only consider the SV centers, it is necessary to account for the volume of the SVs protruding outside the convex hull. To account for this missing volume, we multiplied the convex hull's surface area by the SV radius and added this quantity to the volume of the convex hull. This yielded our final estimated SV cluster volume.

Voronoi Tessellation. The volume associated with each SV within a cluster was determined using Voronoi tessellation with a routine in Scipy. The 3D volumes were generated in Blender. The intersection of each volume with the cluster's Convex Hull was evaluated. The plug-in meshalyzer in Cellblender was used to measure the Voronoi volumes. Only the unaltered Voronoi volumes after calculating the intersection with the Convex Hull and mitochondria were used (a few boutons did not have unaltered Voronoi volume, therefore, they were discarded from the analysis). The final value reported in the manuscript is the Voronoi volume minus the SV volume, referred to as the SV-associated volume.

Center of the SV Cluster and Dispersion. The center of the SV cluster was determined by calculating the mean position of the SVs. Both the center and the distances from the SVs to this center were computed using Python scripts in Blender. To calculate the final distance, the median radius of the SV was subtracted. Additionally, the SD (σ_{xyz}) of the SV positions relative to the cluster's center was assessed. This measurement indicates the dispersion of the SVs from the SV cluster's center.

Dimensionality Reduction and Clustering. To cluster synapses with similar properties PCA in combination with a clustering method was employed. Five features were used for this goal: the distance to neighboring SVs, the SV densities, the dispersion of the SV cluster, and the bouton volume. The data were scaled, centered at zero, and normalized to have a SD of one. Additionally, the data were log transformed prior to performing PCA. The first two principal components capture 90% of the variance. Therefore, these two components were used as input for the K-means algorithm to cluster the boutons. Notably, the bouton volume had the least weight in the PC1 for bouton containing and lacking mitochondria (*SI Appendix*, Table S3 for all the weights).

Random Distribution of SVs in the Cluster. To compare the spatial distribution of SVs, a new distribution was generated for each cluster following a uniform distribution. The 3D-reaction diffusion simulator MCell4 (27) was employed for this purpose. For each SV cluster, the same number of SVs in the bouton were distributed within the convex hull. MCell4 assigned new positions to each SV, which were then imported into Blender to update the 3D locations of the SVs. The methods previously described were also applied to the randomly distributed SVs and the SV-associated volume for each SV was assessed.

Theoretical Calculations and Computer Simulations. Theoretical calculations were used to explore the potential implications of the change in SV density. The diffusion coefficients were determined using theoretical calculations. SVs diffuse within the axon and the SV cluster exhibiting different effective diffusion coefficients. At equilibrium, the number of times SVs hit the boundary surface of the SV cluster (N_{hits}) from inside to outside and from outside to inside should be the same. The equation for the number of hits for a given concentration (C), diffusion coefficient (D), Avogadro number (N_A), time interval (Δt), and surface area (Area) of a given surface has been derived (53) (*SI Appendix*, Eq. **S1**). First, the number of hits from inside the SV cluster to the number of hits from the axon side can be compared for control conditions. The diffusion coefficient of SVs in the cluster has been previously measured [$D_{Control} = 0.05\ \mu m^2\ s^{-1}$ (16)]. In this manner, the diffusion coefficient of SVs in the axon can be estimated (*SI Appendix*, Table S4). Second, assuming the conditions at the axon remain stable during LTP, the number of hits from inside to outside the SV cluster for control and LTP conditions can be compared. This leads to a diffusion coefficient during LTP four times that under control condition (*SI Appendix*, Tables S4 and S5). The theoretical predictions were demonstrated with a reaction–diffusion model built in MCell4, assuming distinct SVs densities and diffusion coefficients in the axon and the SV cluster. Different simulations were conducted for boutons lacking and containing mitochondria, since the densities vary. While the densities vary, the density ratios remain approximately half for both conditions, which implies the changes in diffusion coefficient are similar in boutons containing and lacking mitochondria. For boutons lacking mitochondria, a 50% expansion of the SV cluster was included during LTP. For boutons containing mitochondria, an increase in the total mitochondrial volume was taken into account (parameter values are in *SI Appendix*, Tables S4 and S5).

Data, Materials, and Software Availability. All the software generated during the current study is available in the GitHub repository: https://github.com/guadagar/SV_cluster (54). All other data are included in the manuscript and/or supporting information.

ACKNOWLEDGMENTS. We thank Prof. Mary B. Kennedy for insightful discussion on the formation of condensates in synapses. This work was supported by NSF Technology Hub Award No. 1707356 and NSF NeuroNex2 Award No. 2014862 to K.M.H. and T.J.S., and by NIH grants R01MH095980 and R56MH139176 to K.M.H.

Author affiliations: [a]Computational Neurobiology Laboratory, Salk Institute for Biological Studies, La Jolla, CA 92037; [b]Department of Neuroscience, Center for Learning and Memory, Institute for Neuroscience, University of Texas at Austin, Austin, TX 78712; and [c]Department of Neurobiology, University of California, San Diego, La Jolla, CA 92037

1. T. V. Bliss, T. Lømo, Long-lasting potentiation of synaptic transmission in the dentate area of the anesthetized rabbit following stimulation of the perforant path. *J. Physiol.* **232**, 331–356 (1973).
2. H. R. Monday, T. J. Younts, P. E. Castillo, Long-term plasticity of neurotransmitter release: Emerging mechanisms and contributions to brain function and disease. *Annu. Rev. Neurosci.* **41**, 299–322 (2018).
3. S. Rey, V. Marra, C. Smith, K. Staras, Nanoscale remodeling of functional synaptic vesicle pools in hebbian plasticity. *Cell Rep.* **30**, 2006–2017 (2020).
4. R. Chéreau, G. E. Saraceno, J. Angibaud, D. Cattaert, U. V. Nägerl, Superresolution imaging reveals activity-dependent plasticity of axon morphology linked to changes in action potential conduction velocity. *Proc. Natl. Acad. Sci. U.S.A.* **114**, 1401–1406 (2017).
5. J. N. Bourne, M. A. Chirillo, K. M. Harris, Presynaptic ultrastructural plasticity along ca3→ ca1 axons during long-term potentiation in mature hippocampus. *J. Comp. Neurol.* **521**, 3898–3912 (2013).
6. M. E. Bell *et al.*, Dynamics of nascent and active zone ultrastructure as synapses enlarge during long-term potentiation in mature hippocampus. *J. Comp. Neurol.* **522**, 3861–3884 (2014).
7. L. Kirk *et al.*, Presynaptic vesicles supply membrane for axonal bouton enlargement during ltp. bioRxiv [Preprint] (2025). https://doi.org/10.1101/2025.04.29.651313 (Accessed 5 March 2025).
8. J. H. Jung, L. M. Kirk, J. N. Bourne, K. M. Harris, Shortened tethering filaments stabilize presynaptic vesicles in support of elevated release probability during ltp in rat hippocampus. *Proc. Natl. Acad. Sci. U.S.A.* **118**, e2018653118 (2021).

9. M. D. Applegate, D. S. Kerr, P. W. Landfield, Redistribution of synaptic vesicles during long-term potentiation in the hippocampus. *Brain Res.* **401**, 401–406 (1987).
10. E. Fifková, A. Van Harreveld, Long-lasting morphological changes in dendritic spines of dentate granular cells following stimulation of the entorhinal area. *J. Neurocytol.* **6**, 211–230 (1977).
11. A. Ratnayaka *et al*., Recruitment of resting vesicles into recycling pools supports nmda receptor-dependent synaptic potentiation in cultured hippocampal neurons. *J. Physiol.* **590**, 1585–1597 (2012).
12. X. Chen, X. Wu, H. Wu, M. Zhang, Phase separation at the synapse. *Nat. Neurosci.* **23**, 301–310 (2020).
13. N. A. McDonald, K. Shen, Finding functions of phase separation in the presynapse. *Curr. Opin. Neurobiol.* **69**, 178–184 (2021).
14. N. J. Guzikowski, E. T. Kavalali, Functional specificity of liquid-liquid phase separation at the synapse. *Nat. Commun.* **15**, 10103 (2024).
15. D. Milovanovic, Y. Wu, X. Bian, P. De Camilli, A liquid phase of synapsin and lipid vesicles. *Science* **361**, 604–607 (2018).
16. C. Hoffmann *et al*., Synapsin condensation controls synaptic vesicle sequestering and dynamics. *Nat. Commun.* **14**, 6730 (2023).
17. A. Pechstein *et al*., Vesicle clustering in a living synapse depends on a synapsin region that mediates phase separation. *Cell Rep.* **30**, 2594–2602 (2020).
18. P. Greengard, F. Valtorta, A. J. Czernik, F. Benfenati, Synaptic vesicle phosphoproteins and regulation of synaptic function. *Science* **259**, 780–785 (1993).
19. L. Wang *et al*., α-synuclein multimers cluster synaptic vesicles and attenuate recycling. *Curr. Biol.* **24**, 2319–2326 (2014).
20. L. A. Parra-Rivas *et al*., Serine-129 phosphorylation of α-synuclein is an activity-dependent trigger for physiologic protein-protein interactions and synaptic function. *Neuron* **111**, 4006–4023 (2023).
21. M. Hosaka, R. E. Hammer, T. C. Südhof, A phospho-switch controls the dynamic association of synapsins with synaptic vesicles. *Neuron* **24**, 377–387 (1999).
22. J. N. Bourne, K. M. Harris, Coordination of size and number of excitatory and inhibitory synapses results in a balanced structural plasticity along mature hippocampal ca1 dendrites during ltp. *Hippocampus* **21**, 354–373 (2011).
23. H. L. Smith *et al*., Mitochondrial support of persistent presynaptic vesicle mobilization with age-dependent synaptic growth after ltp. *eLife* **5**, e15275 (2016).
24. E. A. Lazar, J. Lu, C. H. Rycroft, Voronoi cell analysis: The shapes of particle systems. *Am. J. Phys.* **90**, 469–480 (2022).
25. F. Levet *et al*., Sr-tesseler: A method to segment and quantify localization-based super-resolution microscopy data. *Nat. Methods* **12**, 1065–1071 (2015).
26. L. Andronov *et al*., 3dclustervisu: 3d clustering analysis of super-resolution microscopy data by 3d voronoi tessellations. *Bioinformatics* **34**, 3004–3012 (2018).
27. A. Husar *et al*., Mcell4 with bionetgen: A Monte Carlo simulator of rule-based reaction-diffusion systems with python interface. *PLoS Comput. Biol.* **20**, 1–30 (2024).
28. P. Li *et al*., Phase transitions in the assembly of multivalent signalling proteins. *Nature* **483**, 336–340 (2012).
29. S. F. Banani, H. O. Lee, A. A. Hyman, M. K. Rosen, Biomolecular condensates: Organizers of cellular biochemistry. *Nat. Rev. Mol. cell Biol.* **18**, 285–298 (2017).
30. S. Reber, N. W. Goehring, Intracellular scaling mechanisms. *Cold Spring Harb. Perspect. Biol.* **7**, a019067 (2015).
31. W. F. Marshall, Subcellular size. *Cold Spring Harb. Perspect. Biol.* **7**, a019059 (2015).
32. J. W. Posakony, J. M. England, G. Attardi, Mitochondrial growth and division during the cell cycle in hela cells. *J. Cell Biol.* **74**, 468–491 (1977).
33. M. Greenberg, C. Leitao, J. Trogadis, J. Stevens, Irregular geometries in normal unmyelinated axons: A 3d serial em analysis. *J. Neurocytol.* **19**, 978–988 (1990).
34. S. E. Sasaki-Sherrington, J. R. Jacobs, J. K. Stevens, Intracellular control of axial shape in non-uniform neurites: A serial electron microscopic analysis of organelles and microtubules in AI and AII retinal amacrine neurites. *J. Cell Biol.* **98**, 1279–1290 (1984).
35. J. R. Jacobs, J. K. Stevens, Changes in the organization of the neuritic cytoskeleton during nerve growth factor-activated differentiation of pc12 cells: A serial electron microscopic study of the development and control of neurite shape. *J. Cell Biol.* **103**, 895–906 (1986).
36. Y. Shin, C. P. Brangwynne, Liquid phase condensation in cell physiology and disease. *Science* **357**, eaaf4382 (2017).
37. H. Wang *et al*., Live-cell quantification reveals viscoelastic regulation of synapsin condensates by *alpha*-synuclein. *Sci. Adv.* **11**, eads7627 (2025).
38. R. Sansevrino, C. Hoffmann, D. Milovanovic, Condensate biology of synaptic vesicle clusters. *Trends Neurosci.* **46**, 293–306 (2023).
39. T. W. Rosahl *et al*., Essential functions of synapsins i and ii in synaptic vesicle regulation. *Nature* **375**, 488–493 (1995).
40. D. Spillane, T. Rosahl, T. Südhof, R. Malenka, Long-term potentiation in mice lacking synapsins. *Neuropharmacology* **34**, 1573–1579 (1995).
41. S. Chandra *et al*., Double-knockout mice for α-and β-synucleins: Effect on synaptic functions. *Proc. Natl. Acad. Sci. U.S.A.* **101**, 14966–14971 (2004).
42. D. A. Scott *et al*., A pathologic cascade leading to synaptic dysfunction in α-synuclein-induced neurodegeneration. *J. Neurosci.* **30**, 8083–8095 (2010).
43. A. Volianskis *et al*., Different nmda receptor subtypes mediate induction of long-term potentiation and two forms of short-term potentiation at ca1 synapses in rat hippocampus in vitro. *J. Physiol.* **591**, 955–972 (2013).
44. M. J. Devine *et al*., Mitochondrial ca2+ uniporter haploinsufficiency enhances long-term potentiation at hippocampal mossy fibre synapses. *J. Cell Sci.* **135**, jcs259823 (2022).
45. K. M. Harris, Enhanced cycling of presynaptic vesicles during long-term potentiation in rat hippocampus. *J. Physiol.* **603**, 6001–6013 (2025).
46. L. Biasetti *et al*., Elevated amyloid beta disrupts the nanoscale organization and function of synaptic vesicle pools in hippocampal neurons. *Cereb. Cortex* **33**, 1263–1276 (2023).
47. S. Alberti, A. A. Hyman, Biomolecular condensates at the nexus of cellular stress, protein aggregation disease and ageing. *Nat. Rev. Mol. Cell Biol.* **22**, 196–213 (2021).
48. J. C. Fiala, Reconstruct: A free editor for serial section microscopy. *J. Microsc.* **218**, 52–61 (2005).
49. J. C. Fiala, K. Harris, Cylindrical diameters method for calibrating section thickness in serial electron microscopy. *J. Microsc.* **202**, 468–472 (2001).
50. M. A. Chirillo, J. N. Falco, M. D. Musslewhite, L. F. Lindsey, K. M. Harris, Pyreconstruct: A fully open-source, collaborative successor to reconstruct. *Proc. Natl. Acad. Sci. U.S.A.* **122**, e2505822122 (2025).
51. T. M. Bartol *et al*., Computational reconstitution of spine calcium transients from individual proteins. *Front. Synaptic Neurosci.* **7**, 17 (2015).
52. J. Edwards *et al*., Volrovern: Enhancing surface and volumetric reconstruction for realistic dynamical simulation of cellular and subcellular function. *Neuroinformatics* **12**, 277–289 (2014).
53. J. R. Stiles, T. M. Bartol, *Monte Carlo Methods for Simulating Realistic Synaptic Microphysiology Using MCell*, E. Schutter, Ed. (CRC Press, 2001).
54. G. C. Garcia *et al*., SV Cluster. GitHub. https://github.com/guadagar/SV_cluster. Deposited 12 April 2026.